Real-Time Aerosol Optical Properties, Morphology and Mixing States under Clear, Haze and Fog Episodes in the summer of Urban Beijing

Rui Li[1], Yunjie Hu[1], Ling Li[1], Hongbo Fu[1,2,*], Jianmin Chen[1,*]

[1] *Shanghai Key Laboratory of Atmospheric Particle Pollution and Prevention, Department of Environmental Science & Engineering, Fudan University, Shanghai 200433, China Chinese Academy of Sciences, Institute of Atmosphere Physics, Beijing 100029.*

[2] *Collaborative Innovation Center of Atmospheric Environment and Equipment Technology (CICAEET), Nanjing University of Information Science and Technology, Nanjing 210044, China*

Abstract

Aerosol particles play significant roles on the climate-forcing agent via its optical absorption properties. However, the relationship between characteristics of aerosol particles and optical absorption remains poorly understood. Characteristics of aerosol optical properties, morphologies and their relationship were studied in urban Beijing during the clear, haze and fog episodes, sampled from 24th May to 22$_{nd}$ Jun, 2012. Transmission Electron Microscope (TEM), a Cavity Ring Down Spectrometer (CRDS), a nephelometer and an aethalometer were employed to investigate the corresponding changes of the aerosol properties. Five episodes were categorised according to the meteorological conditions and composition. The results showed that the clear episode (EP-2 and EP-4) featured as the low Aerosol Optical Depth (AOD = 0.72) and less pollutants compared with haze (1.14) and fog (2.92) episodes, which are mostly

externally mixed. The high Ångström exponent (> 2.0) suggests that coarse particles were scarcely observed in EP-2 due to the washout of a previous heavy rain, whereas they were widespread in EP-4 (Ångström exponent = 0.04), which had some mineral particles introduced from the north. In contrast, industry-induced haze (EP-1) and biomass burning-induced haze (EP-5) were both affected by the south air mass. Higher AOD values illustrated heavy loading particle concentrations. All of the particles were classified into nine categories including S-rich, N-rich, mineral, K-rich, soot, tar ball, organic, metal and fly ash on the basis of TEM analysis. In the haze episode, as the influence of severe crop residue combustion, a large fraction of soot was detected, which sticks to sulphate or nitrate particles transformed from KCl. The light absorption enhancement was contributed by both black carbon (BC) acceleration, internally mixed effects, and other light absorbing substances. For foggy days, soot was mostly internally mixed with sulphates and nitrates, which revealed themselves after electron exposure under the TEM. The larger size distribution was likely to be caused by both hygroscopic growth and collision between particles during the aging. About 28% of particles were internally mixed in the foggy days, which favored the light absorption. The comparison of all the episodes provides a deeper insight of how mixing states influence the aerosol extinction properties and also a clue to the air pollution control in the crop burning seasons.

Keywords:

Aerosol optical depth, Ångström exponents, Single scattering albedo, Transmission Electron Microscope, Biomass burning, Soot

1. Introduction

Aerosol particles are ubiquitous in the troposphere and exert an important influence on global climate and the environment (Ramana et al., 2010). They affect climate through direct scattering, transmission, and absorption of radiation, or indirectly by acting as nuclei for cloud formation (Buseck and Posfai, 1999). In addition, light extinction by aerosol particles can impair visibility, both during extreme events such as dust storms, and more widely in the vicinity of urban regions, frequently leading to regional haze and fog events (Wang et al., 2009a; Chameides et al., 1999; Sun et al., 2006; Saleh et al., 2016). Common scattering aerosols in the atmosphere include inorganic salts and light-color organic carbon. These aerosols have mainly a "cooling effect" on the climate due to a decrease in the solar radiation that reaches the Earth's surface (Buseck and POsfai, 1999). Soot aerosols, mineral dust, and brown carbon are important absorbing aerosols that can lead to global and regional warming effects (Buseck and POsfai, 1999;Bahadur et al., 2012;Wang et al., 2014). The impact of aerosols on the Earth's climate is a major uncertainty in climate change models as was emphasized in the latest Intergovernmental Panel on Climate Change (IPCC) report (Solomon, 2007). It follows that understanding aerosol optical behaviour and associated spatial and temporal variability is a necessary prerequisite to understanding its role in climate and the environment (Langridge et al., 2012;Che et al., 2014).

Soot is a major contributor to Earth's radiative balance (Ramana et al., 2010). Recent investigations involving direct atmospheric measurements of soot aerosols suggest that they may have a global warming potential second only to CO_2, and the warming effect by soot nearly balances the net cooling effect of other anthropogenic aerosols (Jacobson, 2001). Not

surprisingly, the importance of soot to climate change has been a major focus of many modelling, laboratory, and field studies (Zhang et al., 2008;Adler et al., 2010;Moffet and Prather, 2009;Adachi and Buseck, 2008;Ram et al., 2012). The main uncertainty stems from the fact that the actual amount soot warms our atmosphere strongly depends on the manner and degree in which it is mixed with other species, a property referred to as mixing state (Jacobson, 2001;Moffet and Prather, 2009). The mixing state was found to affect the soot global direct forcing by a factor of 2.9. It has been shown that absorption by soot increases when soot particles are internally mixed and/or coated with other less absorbing materials (Moffet and Prather, 2009). This enhanced absorption in such structure is because of the lensing effect of coated materials (Jacobson, 2001). Field measurements indicate that during transport from the sources, fresh soot becomes internally mixed with sulphate and organics, leading to enhancement in light absorption, which confirms the modelling calculation (Kleinman et al., 2007;Doran et al., 2007;Carabali et al., 2012). Kleinman et al. observed a doubling in the ratio of aerosol light absorption in aged air masses compared to fresh emissions over the eastern U.S. (Kleinman et al., 2007). Similar increases in absorption by soot-bearing aerosol have been reported from ground site measurements performed at a series of locations downwind of Mexico City (Doran et al., 2007). Compiling both the surface and aircraft measurements, Ramana et al. recommended that the solar–absorption efficiency of the Beijing and Shanghai plumes was positively correlated with the ratio of soot to sulphate (Ramana et al., 2010). Lei et al. further confirmed that the enhanced absorption of mixed aerosols depended upon hygroscopicity and the thickness of the coating (Lei et al., 2014). Based on the combined proof

85 from the modelling and field studies, most of researchers proposed that internal mixing models
86 of soot present more realistic absorption estimates as compared to external mixing models in
87 which soot particles coexist with other particles in a physically separated manner (Jacobson,
88 2001;Ramana et al., 2010;Lei et al., 2014).

89 Biomass burning is by far the largest source of primary, fine carbonaceous aerosols in the
90 atmosphere (Habib et al., 2008). It is estimated to contribute 20% of soot aerosols from biomass
91 burning. Besides strongly absorbing soot particles, high amounts of brown organic carbon, such
92 as "tar ball" or HULIS, can be emitted from biomass burning (Roden et al., 2006;Hand et al.,
93 2005;Hoffer et al., 2006). Brown carbon has a significant absorbing component at short
94 wavelengths that may be comparable to the soot absorption (Alexander et al., 2008;Bahadur et
95 al., 2012). Consequently, organic carbon from biomass burning may also contribute to the
96 warming potential of aerosols (Alexander et al., 2008). These large quantities of climate-related
97 aerosols can persist in the atmosphere for several weeks and be transported over long distances.
98 As a result, biomass burning aerosols have a significant impact on climate, which was
99 considered to provide a major uncertainty in accurately predicting the effects of light-absorbing
100 aerosols on the climate (Bahadur et al., 2012). Many field measurements in East Asia, South
101 Asia and Africa have shown extensive biomass burning in these regions causes important
102 perturbations to Earth's atmosphere (Gustafsson et al., 2009; Alexander et al., 2008; Hand et
103 al., 2005). Once biomass burning particles are mixed with other atmospheric components
104 during aging and transport, such as sulfate and dust, solar absorption is further amplified due
105 to the formation of internally mixed particles (Ramanathan et al., 2005). Such mixtures of

106 absorbing and scattering aerosols at the regional scale are referred to as ABCs, for atmospheric
107 brown clouds (Ramanathan et al., 2007). ABCs radiative forcing can cool the surface, stabilize
108 the atmosphere, and reduce evaporation and monsoonal rainfall. The large influence of ABCs
109 on the climate and hydrological cycle changes has recently been demonstrated through model
110 simulations (Ramanathan et al., 2007; Ramanathan et al., 2005).
111 In the farmlands of eastern China such as that near Beijing, most wheat straw is burned in
112 the field within one week after harvesting in preparation for rice cultivation during May and
113 June. Emissions from the biomass burning are often transported and mixed with urban pollution,
114 leading to degradation of air quality, visibility impairment, and regional haze events (Li et al.,
115 2010). Stagnation occurs during episodes of urban haze, when there is insufficient wind
116 velocity to carry pollutants away from the city (Katrinak et al., 1993; Sun et al., 2006). During
117 these periods of pollutant retention, haze particles aggregate continue to collide and combine,
118 resulting in larger average sizes and altered morphology (Li et al., 2010). Enhanced absorption
119 is mainly brought about in the presence of high levels of non-absorbing hygroscopic aerosols
120 such as sulphates, nitrates, and water-soluble organic carbon, as their hygroscopic nature favors
121 internal mixing/core-shell formation (Bahadur et al., 2012). On the other hand, under the
122 condition of high atmospheric relative humidity (RH), the initially hydrophobic soot particles
123 can become associated with hygroscopic materials, leading to increased scattering due to
124 particle growth. At an extreme case, the coating material can cause the absorbing fractal soot
125 to collapse, potentially changing optical behaviour, to further complicate this picture (Zhang et
126 al., 2008; Langridge et al., 2012; Lei et al., 2014; Tan et al., 2016). Such changes cause both

positive and negative effects on the interplay between the direct and indirect aerosol effects, making overall prediction of the radiative forcing difficult. Up to date, large uncertainties exist in estimates of the radiative forcing of haze particles because of the lack of detailed in situ measurements of the mixing state and the associated optical properties as a function of particle size and composition (Moffet and Prather, 2009). These uncertainties limit our ability to quantify the relative impacts of soot on climate, thus limiting our ability to make effective policy decisions.

In an attempt to address this knowledge gap, and in the absence of the opportunity for widespread field studies in eastern China, the experiments in this study were designed to simultaneously measure mixing states and optical properties of haze particles. The present analysis focused on the Beijing plume, which in addition to strong urban emissions is influenced by local agricultural emissions (Li et al., 2010). Light extinction and scattering coefficient was measure with a cavity ring–down spectrometer (CRDs) and a nephelometer, respectively. Absorption was calculated from the difference between extinction and scattering. Individual aerosol particles were identified with transmission electron microscopy (TEM). Back trajectory analyses suggest flow patterns consistent with long-range transport of agricultural smoke to the study site during periods when the sampling site was engulfed by the serious haze and fog.

2. Experimental Sections.

2.1 site description

All of ambient investigation of aerosol optical properties and TEM samplings were conducted at the Institution of Atmospheric Physics (39°58′N, 116°22′N), Beijing, China, from 24th May to 22nd Jun, 2012. Samplers were mounted on the roof of a two-story building about 8 m above ground level. The surroundings are in the convergence of residential and commercial zones with some steel plants locating around in a distance of 6 to 25 km and a waste incineration facility (Gaodun) 8 km in the northeast, which has an operational capacity of 1600 t d^{-1}. In addition, the sampling site is suited in the middle of the North Third Ring Road and North Fourth Ring Road, approximately 360 m south and 380 m north, respectively. The sampling site is impacted by the mixture of residential, industrial, waste combustion and vehicle emissions, but not dominated by any one source.

带格式的：非上标/ 下标

带格式的：非上标/ 下标

2.2 **Cavity ring-down spectrometer and nephelometer**

A self-designed cavity ring-down spectrometer (CRDS) was performed to measure the extinction coefficient of aerosols at 1 min intervals with an accuracy of 0.1 Mm^{-1}. Aerosols were dried by diffusion drying tubes before they reached CRDS and Nephelometer to exclude the influence of relative humidity (RH) on the aerosol optical properties. RH was kept below 40% to minimize the effects of changing RH on measurements. The cavity was formed by two high-reflectivity dielectric mirrors (Los Gatos Research, Inc., Mountain View, CA, USA) and a stainless steel cell equipped with two inlets at both ends and one outlet in the middle. The entire distance of two mirrors is 76.4 cm, while the filling length is 58.0 cm. Dry nitrogen was released near the mirrors at a flow of 0.03 L min^{-1} to prevent the contamination of mirrors and aerosol flow was set 1.0 L min^{-1}. The 532 nm light pulse (energy 100 μJ, duration 11 ns)

was generated by a Q-switched pulsed laser (CrystaLaser QG-532-500). Leaking light through the mirrors was monitored by a Hamamatsu R928 photomultiplier. Details about the system were reported by Li et al (2011). To calculate the decay time, 1000 ring-down traces were averaged at 1000 Hz repetition rate. The extinction coefficient (α_{ext}) has an uncertainty below 3% under the controlled conditions. It was calculated according to the following equation:

$$\alpha_{ext} = \frac{L}{lc}(\frac{1}{\tau} - \frac{1}{\tau_0}) \quad (1)$$

Where L is the length of the cavity, l is effective length occupied by particles, *c* is the speed of light, τ_0 is ring-time time of the cavity filled with particle-free air and τ is the calculated decay time (Li et al., 2011).

An integrating nephelometer (TSI, Model 3563) was operated to obtain aerosol scattering coefficient at three different wavelengths (450, 550, and 700 nm) and the flow rate was set at 5 L min^{-1}. During the field campaign, zero check was done automatically by pumping in particle-free air for 5 min once every 2 h, and a span check was conducted manually using CO_2 as the high span gas and filtered air as the low span gas every week. RH was kept below 40% to minimize the effects of changing RH on measurements (Peppler et al., 2000;Clarke et al., 2007). The raw data were corrected for truncation errors and a non-Lambertian light source using Ångström exponents (å) according to Anderson and Ogren (1998) (Anderson and Ogren, 1998). Generally, the total uncertainty of the scattering coefficient (α_{scat}) was generally below 10%. In accordance with the extinction coefficient at 532 nm, the scattering coefficients was converted to 532 nm ($\alpha_{scat,532}$) on the basis of the following equation:

$$\alpha_{scat,532} = \alpha_{scat,\lambda}(\frac{532}{\lambda})^{-\mathring{a}} \quad (2)$$

Where $\alpha_{scat,\lambda}$ is the scattering coefficient at the wavelength of λ. Accordingly, å could be computed calculated as the equation (3),

$$\mathring{a} = -\frac{\lg(\alpha_{scat,\lambda_1} / \alpha_{scat,\lambda_2})}{\lg(\lambda_1 / \lambda_2)} \quad (3)$$

and the single scattering albedo (ω_0) at the given wavelength could be calculated from equation (4),

$$\omega_0 = \frac{\alpha_{scat}}{\alpha_{ext}} \quad (4)$$

As the sum of absorption (α_{abs}) and scattering (α_{scat}) coefficients equals the extinction coefficient (α_{ext}), α_{abs} could be derived from the equation (5),

$$\alpha_{abs} = \alpha_{ext} - \alpha_{scat} \quad (5)$$

It is known that RH also has a profound impact on visibility (Chow et al., 2002), however, in this study the aerosols passed through a diffusion drying tube before the measurement of optical properties, thus aerosol optical property measurements and TEM observations were both performed in dry condition.

2.3 Aethalometer

An Aethalometer (model AE-31, Magee Scientific Company) was employed to simultaneously quantify BC concentration by calculating the optical attenuation (absorbance) of light from light emitting diode lamps emitting at seven different wavelengths (370, 470, 520, 590, 660, 880 and 950 nm) every 5 minutes, with a typical half-width of 0.02 μm (Hansen, 2003). The flow rate was set to be 5 L min^{-1} and a clean filter canister in the inlet was used weekly to conduct the zero calibration. A $PM_{2.5}$ cyclone (BGI SCC 1.828) was employed in the sampling line with a flow rate of 5 L min^{-1}. A typical noise level is less than 0.1 μg cm^{-3} on a 5-min basis. Two photo-detectors monitor the light intensity as a function of time. One measured the light intensity of the light crossing reference quartz filter, while the other measured that of the same light crossing a sample spot under the identical conditions. The wavelength at 880 nm was used to derive the aerosol absorption coefficient (σ_{abs}). Then BC concentration could be converted under the assumption that the BC mass concentration [BC] on the filter was linearly correlated to the aerosol absorption coefficient, as the following equation (6),

$$\sigma_{abs} = \alpha[BC] \quad (6)$$

Where [BC] is the BC mass concentration, and α is a conversion factor. A factor of 8.28 m^2 g^{-1} was employed to convert the aerosol absorption coefficient to BC concentration, according to the results of inter-comparison experiment conducted in south China (Wu et al., 2009;Yan et al., 2008).

The uncertainty of measurement might originate from the multiple scattering in the filter fibres in the unloaded filter and in those particles embedded in the filters (Clarke et al., 2007;Jeong et al., 2004). The

attenuation values were within the limit of an acceptable uncertainty, that is, no greater than 150 in the range of 75-125 at various wavelengths, verifying the reliability of the measurement. Moreover, the BC concentration was compared with the results of multi-angle absorption photometry (MAAP, Model-5012) and a particle soot absorption photometer (PSAP, Radiance Research), which shows great consistence.

2.4 Aerosol optical depth

Aerosol optical depth (AOD) data at the sampling site was based on the MODIS (Moderate Resolution Imaging Spectroradiometer) retrieved data from a CIMEL CE-318 sunphotometer (AERONET/PHOTONS) at Institute of Atmospheric Physics, reflecting the amount of direct sunlight prevented from reaching the ground by aerosol particles by measuring the extinction of the solar beam. The AOD value of the sampling site was downloaded from the AERONET (http://aeronet.gsfc.nasa.gov), using the Level 2.0. Quality Assured Data. These data are pre and post field calibrated, automatically cloud cleared and manually inspected. The regional distribution of AOD was obtained from Giovanni (GES-DISC Interactive Online Visualization And Analysis Infrastructure) maps from MODIS satellite data (http://disc.sci.gsfc.nasa.gov/giovanni). Two continuous episodes featuring as clear and haze are chosen, 23th May to 27th May and 19th June to 27th June, respectively.

2.5 TEM Analysis

Samples were made by collecting air-borne particles onto copper TEM grids coated with carbon film (carbon type-B, 300-mesh copper, Tianld Co., China) using a single-stage cascade impactor with a 0.5 mm diameter jet nozzle at a flow rate of 1.0 $L \cdot min^{-1}$. According to the visibility, the sampling time varies from 1 min to 10 min. 3 or 4 samples were collected each morning at around 8 am and also each time when haze or fog appeared. After collection, samples were stored in a dry plastic box sealed in a plastic bag and kept in a desiccator at 25 ℃ and 20 ± 3%. Details of the analysed samples, such as sampling time and instantaneous meteorological state are listed in Table 1.

Individual aerosol samples were analysed using a high resolution TEM (JEOL 2010, Japan) operated at 200 kV. TEM can obtain morphology, size, and mixing state of individual aerosol particles. Energy-dispersive X-ray spectrometer (EDS) can get the chemical compositions of the targeted particles. Cu and C

were excluded from the copper TEM grid with carbon film. Details have been described in the previous paper (Fu et al., 2012; Guo et al., 2014a). Particle sizes on the grid decrease from the centre to the periphery due to the limitation of sampler, and three to four round meshes were chosen from the centre to the periphery in a line to ensure the representative of the entire size range. Each mesh analyses three to four views. The average values of each mesh were used for statistics. The analysis was done by labour-intensive manual sortation of the particles. 9 grids, all of 1173 particles have been analysed by TEM.

2.6 Back trajectories and meteorological data

NOAA/ARL Hybrid Single-Particle Lagrangian Integrated Trajectory model (available at http://www.arl.noaa.gov/ready/hysplit4.html) was employed to determine back trajectories arriving at Beijing at 100 m, employing the data of global data assimilation system (GDAS). Each trajectory represented the past 72 h of the air mass, with its arrival time at 00:00 UTC every day.

Meteorological data was downloaded from Weather Underground (www.wunderground.com), and Daily PM_{10} values were transformed from daily API (Air Pollutant Index) in the datacentre of ministry of Environmental Protection of the People's Republic of China (http://datacenter.mep.gov.cn/).

3. Results and Discussion

3.1 Episode segregations

Haze was usually defined as a weather phenomenon that lasts a duration of at least 4 h when the visibility is less than 10 km and RH lower than 80% (Sun et al., 2006), while fog was characterized with a higher RH, larger than 90%, according to the Chinese Meteorological Administration. The sampling period was categorized into 5 episodes to observe the optical properties between different weather phenomena (Fig. 1). Although every episode contains a mixture of different pollutions, the main origin can be discerned by studying the weather condition, back trajectories and fire maps. The 1st episode (EP-1) was from 28th May to 29th May, when a haze occurred with the south wind bringing in the industrial pollution from the heavily polluted cities in the south, which conformed to the 3-day back trajectories shown in Fig. 2a, showing the air masses passing through Henan, Shandong, Hebei and Tianjin before arriving at the sampling site. Only scattered fire spots were observed during these days along the air mass pathway, suggesting little biomass

burning emission interference. The 2nd episode (EP-2) was in clear weather on 30th May. A heavy rain interrupted the previous haze; hence the air were cleaned up by rain washout. It was impacted by the air mass from the north region (Fig. 2b), as the north wind was relatively clean and the time was insufficient for a heavy accumulation. This episode could be viewed as the background. The 3rd episode (EP-3) from 31st May to 9th Jun was fickle, with a variety of transitions between fog, haze and clear days. This was partly caused by the variable wind directions and air mass transferring (Fig. 2c). When the wind is from east, the back trajectories are across the Bohai Sea, and the air mass carries a high content of water vapour, facilitating the formation of fog, whereas when south wind is dominant, haze is likely to occur (Wang and Chen, 2014;Zhang et al., 2010). The following 4th episode (EP-4) from 10th Jun to 16th Jun is mainly clear days with slight dust. Their back trajectories originate from the north part (Fig. 2d), and mostly travelling from the Siberian region, across eastern Mongolia and Inner Mongolia and finally arriving the sampling site with little pollution. The last episode (EP-5) was from 17th Jun to 21st Jun. Severe haze was observed during this duration. Fig. 2e shows that the air parcel pathway across by dense fire spots, indicating a severe impact of the biomass burning. Every year after harvest, crop residue burning is extremely frequent in Anhui, Shandong and Henan provinces as they served as important centres for the rice supply (Li et al., 2010). Therefore, the biomass burning emissions can be the main contributor to the haze formation in this episode.

3.2 Optical parameter variation

Aerosol optical depth (AOD) is representative of the airborne aerosol loading in the atmospheric column，which was also verified by a significant related coefficient with PM_{10} (R_I=0.603) (Fig. 1). The overall AOD is contributed by both Mie scatter and Rayleigh scatter (Fig. 3a). The former one is produced by the scatter effect of particles while the latter one by gases (Brown et al., 2014). The data shown in Fig. 1 demonstrates that gas plays a negligible role in the AOD value, especially when aerosol loading is high. Apparently, the AOD value varied with the weather transition. During the clean days, the mean AOD was 0.723, while it became higher when the haze and fog were formed, with a mean value of 2.92 and 1.14, respectively.

During the measurement period, AOD reached its highest value of 5.0 in the hazy EP-5, which was much higher by 5 times than the average AOD of 0.95 in Beijing measured from Mar 2012 to Feb 2013 (Guo et al., 2014b). Such high AOD could be attributed to the pollutant accumulation, especially biomass burning emission from the crop combustion.

Ångström exponent (å) is a good indicator of aerosol size distribution, which decreases with the increase of particle size (Eck et al., 1999). The value is computed from pairs of AOD measurements at 700 nm with 450 nm, 700 nm with 550 nm and 550 nm with 450 nm, respectively. A high accordance is observed between each pair (Fig. 3b). The å increases sharply to its highest value above 2.0 at EP-2, 45 times of the minimum value 0.044 observed in EP-5. This could be explained by the wet removal impact of the heavy rain. It is well known that rains wash out the coarse particles, resulting in a fine size distribution (Dey et al., 2004). The å value during EP-4 fluctuated between 0.08 and 0.2. Since the rains are light and short, the clear days in EP-4 are more impacted by the north air mass, which brings in a larger fraction of coarse dust particles. Comparatively, the å value was lower in both the haze and fog periods including EP-1, EP-3 and EP-5. Especially in the case of EP-5, the low å value indicated that the biomass burning emission could contain more coarse particles. Such scene is in contrast to the conclusion that the haze days were dominated by fine particles (Yan et al., 2008). It is likely caused by the high collision occurrences of fine particles along the long-range transport from the fire spots (Wang et al., 2009b). In comparison, the å value during 2001 to 2005 in Beijing altered between 0.04 and 1.06 (Yu et al., 2006). The lower limit is similar with the present field-measurement, while the upper limit is much higher than this study. This could be attributed to the increase of fine particle emission contributed by more vehicles, waste incineration and industrial plants in the past years.

Single scattering albedo (SSA), ω, was defined as the ratio of the aerosol scattering coefficient (σ_{sca}) to the extinction coefficient (σ_{ext}). This parameter is especially important in the estimation of direct aerosol radiative forcing, since even a small error in its estimation might change the sign of aerosol radiative forcing (Takemura et al., 2002). Figs. 3c and d show the time series of σ_{sca}, σ_{abs}, σ_{ext} and SSA at 550 nm during the

measurement period. The mean ω was 0.73, 0.82 and 0.79 in EP-2, EP-4, and EP-5, respectively, implying that mineral dust in EP-4 accelerates the optical scattering while soot favours the optical absorption. Compared with other reported results (Che et al., 2014; Li et al., 2007; Qian et al., 2007), the mean ω is lower in this study, suggesting that more soot is uploaded into the atmosphere during this period. It is well known that soot emission is much higher in the past years, mainly contributed by the residential coal combustion, biomass burning, coke production, and diesel vehicles (Wang et al., 2012b). Especially, when air masses moved from south direction the sampling site were influenced by heavy polluted air mass mixed by soot, sulfate, and OC-components, from the dense population centres and industrial areas (Sun et al., 2006;Wang et al., 2006), which was also confirmed by the TEM observation.

3.3 TEM analysis

Based on morphology and chemical composition, 1173 particles were classified into nine categories: S-rich (Fig. 4a), N-rich (Fig. 4b), mineral (Fig. 4c), K-rich (Fig. 4d), soot (Fig. 4e), tar ball (Fig.4f), organic (Fig.4g), metal (Fig. 4h) and fly ash (Fig. 4i). The classification is similar to the work reported by Li and Shao (2009).

The most common particles are sulphates and nitrates (Figs. 4a and b), which are of the size around 1.0 μm, and have a light scattering ability (Jacobson, 2001). Sulphates appeared as subrounded masses under the TEM, which decomposed or evaporated under the electron beam exposure. Conventionally, they were formed by the reaction of precursor SO_2 or H_2SO_4 with other gases or particles (Khoder, 2002). Nitrates were mostly of scalloped morphology in the TEM images. They were relatively stable when exposed to the electron beam. Nitrates formed through the homogeneous reaction with the precursor either NO_2 or heterogenic reaction with HNO_3 (Khoder, 2002). (Pathak et al., 2004; Seinfeld and Pandis, 2012).

In the clear days, as the result of effects of northern air mass, dust particles were relatively abundant. The size of dust particles (Fig. 4c) were large, usually bigger than 1.0 μm, so far as to 8.0 μm. Their compositions differed from each other, mostly are silicates and calcium sulphate or carbonate, all of which were stable under the exposure of the electron beam. Dust particles were reported to have a light scattering effect,

resulting in a negative aerosol radiative forcing (Wang et al., 2009b). They took up a large portion in EP-4, impacted by the north wind taking along particles from the dusty regions.

As for the haze episode, K-rich particles (Li et al., 2010; Duan et al., 2004; Engling et al., 2009), soot (Li et al., 2010), tar ball (Chakrabarty et al., 2010;Bond, 2001) and organic (Lack et al., 2012) were more observed under the TEM. K-rich particles (Fig. 4d) often existed as sulphate or nitrate. A larger fraction of K-rich particles was observed in EP-5 than those in the other periods. Together with the back trajectories and fire spot maps, it was supposed that the regional haze occurred in EP-5 was contributed significantly by the biomass burning. K-rich particles were characterized by the irregular shape, which was unstable when exposed to electron beam. KCl was barely detected in the samples, even though it has been recommended that KCl was internally mixed with K_2SO_4 and KNO_3 in fresh biomass burning plumes (Li et al., 2010;Li et al., 2003;Adachi and Buseck, 2008). Based on the EDS data, K-rich particles in the present work mostly consisted of N, Na, O, S, and K, whereas it was free of Cl, implying KCl could have suffered from chemical reactions and transformed into sulphates or nitrates (Li and Shao, 2010). Such particles displayed a negative climate forcing (Hauglustaine et al., 2014).

It was well documented that soot (Fig. 4e) was vital to light absorption, which could alter regional atmospheric stability and vertical motions, the large scale circulation and precipitation with significant regional climate effects (Ramanathan et al., 2001;Jacobson, 2002). It was well characterized by a structure like onion ring, resembling a fractal long chain as agglomerates of small spherical monomers (Li and Shao, 2009). The fresh soot was loose and externally mixed. However, after undergoing a long-range transportation and aging in the atmosphere, soot became more compacted, with a slight increase of O concentration because of the photochemistry (Stanmore et al., 2001; Krasowsky et al., 2016). Meanwhile, soot generally attached to other particles on the surface or serves as the core for other particle formation.

Tar ball (Fig. 4f) was present as a spherical carbon ball with a small fraction of O. It was thought to origin from the smouldering combustion and have relatively strong absorption effects (Chakrabarty et al., 2010; Bond, 2001). Tar balls constituted a large fraction of the fresh emitted wildfire carbonaceous particles (China et al., 2013;Lack et al., 2012). But it was seldom observed in the present work, even in EP-5 when

371 there was severe biomass burning emission, which may be due to the difference in burning species and
372 conditions.

373 Organic matter (Fig. 4g) identified by HRTEM was amorphous species, and was stable under the strong
374 electron beam exposure. It could be traced to the direct emission such as biomass burning (Lack et al.,
375 2012), or the second reaction between VOCs with ozone (Wang et al., 2012a). It can absorb radiation in the
376 low-visible and UV wavelengths (Chakrabarty et al., 2010;Clarke et al., 2007;Lewis et al., 2008;Hoffer et
377 al., 2006). In addition, when compassing soot as the core, organic matter can enhance absorption by internal
378 mixing (Adachi and Buseck, 2008).

379 For the common haze and fog episodes, the stagnated weather favours the accumulation of pollutants,
380 especially metal particles and fly ash (Hu et al., 2015). Metal particles (Fig. 4h) were generally round and
381 stable under the TEM. Fly ash (Fig. 4i) was a dark sphere with large size of > 1 μm. It was a common
382 product of industrial activities in the northern China (Shi et al., 2003). As the complex refractive index
383 (CRI) indicated, metal oxide particles and fly ash can scatter light, but the former has a weak absorption
384 ability while the later has almost no light absorption ability (Ebert et al., 2004).

385 Figure 5 shows percentage of nine components in clear, haze and fog episodes under external mixing,
386 internal mixing and adjacent states (partially internal mixing). About 28% of particles were internally mixed
387 in the foggy days, while about 52% of particles exhibited external mixing state in clear days based on the
388 TEM analysis. Mineral particles were inclined to be externally mixed with K-rich particles and organic
389 matter in clear days, while the external ratio of other particles were relatively lower, particularly in the haze
390 and fog days. Li et al. (2010) showed that mineral particles generally displayed external association with
391 organic matter or other particles. However, many fine particles including metal-bearing particles, fly ash
392 and soot were often internally mixed with S-rich and K-rich particles, particularly during the fog-haze
393 episodes. Shi et al. (2008) reported that rapid aging of fresh soot tended to appear during the fog-haze days,
394 which were generally associated with ammonium sulfate. Heavy polluted air generally promoted the
395 coagulation between S/K-rich particles and those fine particles such as metal particles, soot, and fly ash (Li

and Shao, 2009), which could explain the results. Additionally, haze and fog episodes held a higher possibility of collision and attachment due to the heavy particle loading and prolonged remaining in the atmosphere, leading to a higher internal mixed state percentage around 65%.

3.4 The relation of optical properties and the morphologies of aerosol particles

The different morphologies of the particles collected from the different weather can be easily identified under the TEM, as shown in Fig. 6. Due to the washout effect of the heavy rain, the particles collected in the typical clear period of EP-2 were much smaller in size (Figs. 6a, b), which was in good agreement with the larger Ångström exponent. The coarse particles, such as dusts, were hardly observed, whereas a few K-rich particles were detected, of which presented in small cubic shape. Such particles could be explained by the coal combustion around the sampling site due to the slight fire spots presence. Besides, the cubic shape of K-rich particles suggested they have not undergone long transportation or severe photochemical reaction because cubic K-rich particles were generally generated from the molten nature of the material at high temperatures (Ault et al., 2012). Likewise, soot was generally less oxidized in the EP2 periods, maintaining fractional morphologies and externally mixed. Small metal particles and amorphous Zn-particles dominated the fine particles, which was ascribed to the industrial activity and/or waste incineration (Choël et al., 2006;Moffet et al., 2008).

In the EP-5 episode, the increased aerosol loading played a remarkable role in the enhancement of scattering coefficient and decrease of visibility (Kang et al., 2013;Charlson et al., 1987;Deng et al., 2008). Because of the high rate of aerosol collision, particles were larger than those in the clear days (Figs. 6c, d), leading to a smaller Ångström exponent. Almost of the soot particles observed under the TEM were compact and adhesive. It was internally mixed with the K-rich particles, which were larger, rounder or with a coating of high S components. As discussed above, they were probably transported from the south crop residual burning and undergo the ageing in the atmosphere, confirmed by the trajectories passing through intense fire spots. Due to the high concentration of soot, EP-5 were characterized by a high absorption coefficient, shown in Fig. 3.

The BC variations in the different weather types during the sampling period were illustrated in Fig. 7. The preliminary component of BC could be viewed as the soot. High BC concentration was easily recognized in EP-5 with a mean value of 12.8 μg m^{-3}, while it is low up to 1.04 μg/m^3 during the clear periods. The former is about 11.3 times higher than that of the latter, which is due to the lower boundary layer. In comparison, absorption coefficient of EP-5 (468.7 Mm^{-1}) was about 94.7 times higher than that of EP-4 (1.3 Mm^{-1}), more than 8 times of the BC ratio. It was supposed that BC was internally mixed with other aerosols in the EP-5, which lead to the considerable elevation of absorption coefficient (Tan et al., 2016). However, ~~Models~~ models estimated an enhancement of BC forcing up to a factor of 2.9 when BC is internally mixed with other aerosols, compared with externally mixed scenarios (Jacobson, 2001), which was much lower than this case. Accordingly, other light absorbing substances may contribute to the discrepancy. For example, ~~Brown~~ brown carbon is an indispensable component of biomass burning, which has a strong absorption ability as well (Hoffer et al., 2006;Andreae and Gelencsér, 2006). Other particles ~~like~~ such as dust may also contribute to the over-enhanced absorption coefficient (Yang et al., 2009). Our observations were agreement with the previous studies reported by (Wang et al., 2009b; Xia et al., 2006), which shows that aerosol particles under hazy weather conditions generate a positive heating effect on the atmospheric ~~column (Wang et al., 2009b;Xia et al., 2006).~~

In the foggy days of EP-3 episode, the high PM_{10} concentration and AOD caused significant increase of scattering coefficient (Tan et al., 2016). Furthermore, metal-bearing particles and soot were internally associated with some coatings including S-rich, N-rich and K-rich particles. Zhang et al. (2008) reported that coating with sulphuric acid enhance the optical properties of soot aerosols. Furthermore, the collected particles displayed larger size than those collected from the clear days under the TEM (Figs. 6e, f). The larger size particles in the foggy days could be caused by hydroscopic growth under the high relative humidity, and the collision among the overloading particles, which was likewise illustrated by the Ångström exponent shown in Fig.3. Consequently, the larger particles enhance the scattering of sunlight, and lead to more apparent impairment of visibility (Quan et al., 2011). Chow et al. (2002a) reported that RH also has a profound impact on visibility. Some fan-like nitrate particles have inclusions which may act as the growth

带格式的：非突出显示

cores or be encompassed during the hydroscopic growth. Bian et al. (2009) reported that whenever the RH is elevated, its importance to AOD is substantially amplified if the particles are hygroscopic (Bian et al., 2009). Li et al. (2010) found that soot particles became hydrophilic when they were coated with the water-soluble compounds such as sulphates or nitrates, implying that soot can provide important nuclei for the development of aerosol particles. Furthermore, Fig. 6e and f illustrate a large fraction of internally mixed soot. It was not visible until being exposed to electron beam for a short time. As for an internally mixed particle, sulphate and nitrate coatings act as a "focusing mirror", and enhanced light absorption greatly. Therefore, the BC concentration in foggy conditions was 6.12 $\mu g\ m^3$, and the absorption coefficient is 143.7 Mm^{-1}, which were 2.09 and 0.83 times of the hazy days, respectively. Model calculation also have recommended that light absorption ability of the internally mixed soot particles were enhanced by 30% than that of soot alone (Fuller et al., 1999). A variety of metal particles were also observed in the foggy days, as foggy days had a stable low upper layer boundary and slight wind, leading to the accumulation of pollutions. These pollution sources range from steel plants and waste incineration to vehicle emission and so on (Hu et al., 2015).

4 Conclusions

The relationship between characteristics of aerosol particles and optical properties is of importance to the atmospheric chemistry research. However, the relationship between characteristics of aerosol particles and optical absorption remains poorly understood. Characteristics of aerosol optical properties, morphologies and their relationship were studied in urban Beijing during the clear, haze and fog episodes, sampled from 24th May to 22nd Jun, 2012. Transmission Electron Microscope (TEM), a Cavity Ring Down Spectrometer (CRDS), a nephelometer and an aethalometer were employed to investigate the corresponding changes of the aerosol properties. Five episodes were categorised according to the meteorological conditions and composition. The results indicated that the clear episode (EP-2 and EP-4) was characterized as the low aerosol Optical Depth (AOD = 0.72) and less pollutants compared with haze (1.14) and fog (2.92) episodes, which are mostly externally mixed. The high Ångström exponent (> 2.0) suggests that coarse particles were scarcely observed in EP-2 due to the washout of a previous heavy rain, whereas they were

widespread in EP-4 (Ångström exponent = 0.04), which had some mineral particles introduced from the north. In contrast, industry-induced haze (EP-1) and biomass burning-induced haze (EP-5) were both affected by the south air mass. Higher AOD values illustrated heavy loading particle concentrations. All of the particles were classified into nine categories including S-rich, N-rich, mineral, K-rich, soot, tar ball, organic, metal and fly ash based on the TEM analysis. In the haze episode, as the influence of severe crop residue combustion, a large fraction of soot was detected, which sticks to sulphate or nitrate particles transformed from KCl. Both black carbon (BC) acceleration, internally mixed effects, and other light absorbing substances, contributed the light absorption enhancement. For foggy days, soot was mostly internally mixed with sulphates and nitrates, which revealed themselves after electron exposure under the TEM. The larger size distribution was likely to be caused by both hygroscopic growth and collision between particles during the aging. About 28% of particles were internally mixed in the foggy days, which favored the light absorption. The comparison of all the episodes provides a deeper insight of how mixing states influence the aerosol extinction properties and also a clue to the air pollution control in the crop burning seasons. The result presented herein is beneficial to air pollution control and prevention in China.

ACKNOWLEDGMENTS

This work was supported by National Natural Science Foundation of China (Nos. 21577022, 21190053, 40975074), Ministry of Science and Technology of China (2016YFC0202700), and International cooperation project of Shanghai municipal government (15520711200).

References

Adachi, K., and Buseck, P.: Internally mixed soot, sulfates, and organic matter in aerosol particles from Mexico City, Atmos. Chem. Phys., 8, 6469-6481, 2008.

Adler, G., Riziq, A. A., Erlick, C., and Rudich, Y.: Effect of intrinsic organic carbon on the optical properties of fresh diesel soot, P. Natl. Acad. Sci. USA., 107, 6699-6704, 2010.

Alexander, D. T., Crozier, P. A., and Anderson, J. R.: Brown carbon spheres in East Asian outflow and their optical properties, Science, 321, 833-836, 2008.

带格式的：字体：11 磅

498 Anderson, T. L., and Ogren, J. A.: Determining aerosol radiative properties using the TSI 3563 integrating
499 nephelometer, Aerosol Air Qual. Res., 29, 57-69, 1998.
500 Andreae, M., and Gelencsér, A.: Black carbon or brown carbon? The nature of light-absorbing
501 carbonaceous aerosols, Atmos. Chem. Phys., 6, 3131-3148, 2006.
502 Ault A.P., Peters T.M., Sawvel E.J., Casuccio G.S., Willis R.D., Norris G.A., et al.: Single-particle SEM-
503 EDX analysis of iron-containing coarse particulate matter in an urban environment: sources and distribution
504 of iron within Cleveland, Ohio. Environ Sci Technol., 46: 4331–4339, 2012.
505 Bahadur, R., Praveen, P. S., Xu, Y., and Ramanathan, V.: Solar absorption by elemental and brown carbon
506 determined from spectral observations, P. Natl. Acad. Sci. USA., 109, 17366-17371, 2012.
507 Bian, H., Chin, M., Rodriguez, J., Yu, H., Penner, J. E., and Strahan, S.: Sensitivity of aerosol optical
508 thickness and aerosol direct radiative effect to relative humidity, Atmos. Chem. Phys., 9, 2375-2386, 2009.
509 Bond, T. C.: Spectral dependence of visible light absorption by carbonaceous particles emitted from coal
510 combustion, Geophys. Res. Lett., 28, 4075-4078, 2001.
511 Brown, A.J.: Spectral bluing induced by small particles under the Mie and Rayleigh regimes, Lcarus., 239,
512 85-95, 2014.
513 Buseck, P. R., and POsfai, M.: Airborne minerals and related aerosol particles: Effects on climate and the
514 environment, P. Natl. Acad. Sci. USA., 96, 3372-3379, 1999.
515 Carabali, G., Mamani-Paco, R., Castro, T., Peralta, O., Herrera, E., and Trujillo, B.: Optical properties,
516 morphology and elemental composition of atmospheric particles at T1 supersite on MILAGRO campaign,
517 Atmos. Chem. Phys., 12, 2747-2755, 2012.
518 Chakrabarty, R., Moosmüller, H., Chen, L.-W., Lewis, K., Arnott, W., Mazzoleni, C., Dubey, M., Wold,
519 C., Hao, W., and Kreidenweis, S.: Brown carbon in tar balls from smoldering biomass combustion, Atmos.
520 Chem. Phys., 10, 6363-6370, 2010.
521 Chameides, W. L., Yu, H., Liu, S., Bergin, M., Zhou, X., Mearns, L., Wang, G., Kiang, C., Saylor, R., and
522 Luo, C.: Case study of the effects of atmospheric aerosols and regional haze on agriculture: An opportunity

带格式的：字体：11 磅

带格式的：字体：11 磅

to enhance crop yields in China through emission controls?, P. Natl. Acad. Sci. USA., 96, 13626-13633, 1999.

Charlson, R. J., Lovelock, J. E., Andreae, M. O., and Warren, S. G.: Oceanic phytoplankton, atmospheric sulphur, cloud albedo and climate, Nature, 326, 655-661, 1987.

Che, H., Xia, X., Zhu, J., Li, Z., Dubovik, O., Holben, B., Goloub, P., Chen, H., Estelles, V., and Cuevas-Agulló, E.: Column aerosol optical properties and aerosol radiative forcing during a serious haze-fog month over North China Plain in 2013 based on ground-based sunphotometer measurements, Atmos. Chem. Phys., 14, 2125-2138, 2014.

China, S., Mazzoleni, C., Gorkowski, K., Aiken, A. C., and Dubey, M. K.: Morphology and mixing state of individual freshly emitted wildfire carbonaceous particles, Nature commun., 4, 2013.

Choël, M., Deboudt, K., Flament, P., Lecornet, G., Perdrix, E., and Sobanska, S.: Fast evolution of tropospheric Pb-and Zn-rich particles in the vicinity of a lead smelter, Atmos. Environ., 40, 4439-4449, 2006.

Chow, J. C., Bachmann, J. D., Wierman, S. S., Mathai, C., Malm, W. C., White, W. H., Mueller, P. K., Kumar, N., and Watson, J. G.: Visibility: science and regulation, J. Air. Waste Manage., 52, 973-999, 2002.

Clarke, A., McNaughton, C., Kapustin, V., Shinozuka, Y., Howell, S., Dibb, J., Zhou, J., Anderson, B., Brekhovskikh, V., and Turner, H.: Biomass burning and pollution aerosol over North America: Organic components and their influence on spectral optical properties and humidification response, J. Geophys. Res.-Atmos., 112, 2007.

Deng, X., Tie, X., Wu, D., Zhou, X., Bi, X., Tan, H., Li, F., and Jiang, C.: Long-term trend of visibility and its characterizations in the Pearl River Delta (PRD) region, China, Atmos. Environ., 42, 1424-1435, 2008.

Dey, S., Tripathi, S. N., Singh, R. P., and Holben, B. N.: Influence of dust storms on the aerosol optical properties over the Indo-Gangetic basin, J. Geophys. Res.-Atmos., 109, 10.1029/2004jd004924, 2004.

Doran, J., Barnard, J. C., Arnott, W., Cary, R., Coulter, R., Fast, J. D., Kassianov, E. I., Kleinman, L., Laulainen, N. S., and Martin, T.: The T1-T2 study: evolution of aerosol properties downwind of Mexico City, Atmos. Chem. Phys., 7, 1585-1598, 2007.

549 Duan, F., Liu, X., Yu, T., and Cachier, H.: Identification and estimate of biomass burning contribution to
550 the urban aerosol organic carbon concentrations in Beijing, Atmos. Environ., 38, 1275-1282, 2004.
551 Ebert, M., Weinbruch, S., Hoffmann, P., and Ortner, H. M.: The chemical composition and complex
552 refractive index of rural and urban influenced aerosols determined by individual particle analysis, Atmos.
553 Environ., 38, 6531-6545, 2004.
554 Eck, T. F., Holben, B. N., Reid, J. S., Dubovik, O., Smirnov, A., O'Neill, N. T., Slutsker, I., and Kinne, S.:
555 Wavelength dependence of the optical depth of biomass burning, urban, and desert dust aerosols, J.
556 Geophys. Res.-Atmos., 104, 31333-31349, 10.1029/1999jd900923, 1999.
557 Engling, G., Lee, J. J., Tsai, Y.-W., Lung, S.-C. C., Chou, C. C.-K., and Chan, C.-Y.: Size-resolved
558 anhydrosugar composition in smoke aerosol from controlled field burning of rice straw, Aerosol Air Qual.
559 Res., 43, 662-672, 2009.
560 Fu, H., Zhang, M., Li, W., Chen, J., Wang, L., Quan, X., and Wang, W.: Morphology, composition and
561 mixing state of individual carbonaceous aerosol in urban Shanghai, Atmos. Chem. Phys., 12, 693-707, 2012.
562 Fuller, K. A., Malm, W. C., and Kreidenweis, S. M.: Effects of mixing on extinction by carbonaceous
563 particles, J. Geophys. Res.-Atmos., 104, 15941-15954, 1999.
564 Guo, L., Hu, Y., Hu, Q., Lin, J., Li, C., Chen, J., Li, L., and Fu, H.: Characteristics and chemical
565 compositions of particulate matter collected at the selected metro stations of Shanghai, China, Sci. Total
566 Environ., 496, 443-452, 2014a.
567 Guo, Y., Feng, N., Christopher, S. A., Kang, P., Zhan, F. B., and Hong, S.: Satellite remote sensing of fine
568 particulate matter ($PM_{2.5}$) air quality over Beijing using MODIS, Int. J. Remote Sens., 35, 6522-6544, 2014b.
569 Gustafsson, Ö., Kruså, M., Zencak, Z., Sheesley, R. J., Granat, L., Engström, E., Praveen, P., Rao, P., Leck,
570 C., and Rodhe, H.: Brown clouds over South Asia: biomass or fossil fuel combustion?, Science, 323, 495-
571 498, 2009.
572 Habib, G., Venkataraman, C., Bond, T. C., and Schauer, J. J.: Chemical, microphysical and optical
573 properties of primary particles from the combustion of biomass fuels, Environ. Sci. Technol., 42, 8829-
574 8834, 2008.

575 Hand, J. L., Malm, W., Laskin, A., Day, D., Lee, T.-b., Wang, C., Carrico, C., Carrillo, J., Cowin, J. P., and
576 Collett, J.: Optical, physical, and chemical properties of tar balls observed during the Yosemite Aerosol
577 Characterization Study, J. Geophys. Res.-Atmos., 110, 2005.
578 Hansen, A.: The Aethalometer Manual, Magee Sci., Berkeley, Calif, 2003.
579 Hoffer, A., Gelencsér, A., Guyon, P., Kiss, G., Schmid, O., Frank, G., Artaxo, P., and Andreae, M.: Optical
580 properties of humic-like substances (HULIS) in biomass-burning aerosols, Atmos. Chem. Phys., 6, 3563-
581 3570, 2006.
582 Hu, Y., Lin, J., Zhang, S., Kong, L., Fu, H., and Chen, J.: Identification of the typical metal particles among
583 haze, fog, and clear episodes in the Beijing atmosphere, Sci. Total Environ., 511, 369-380, 2015.
584 Hauglustaine, D.A., Balkanski, Y., Schulz, M.: A global model simulation of present and future nitrate
585 aerosols and their direct radiative forcing of climate, Atmos. Chem. Phys., 14, 6863-6949, 2014.
586 Jacobson, M. Z.: Strong radiative heating due to the mixing state of black carbon in atmospheric aerosols,
587 Nature, 409, 695-697, 2001.
588 Jacobson, M. Z.: Control of fossil‐fuel particulate black carbon and organic matter, possibly the most
589 effective method of slowing global warming, J. Geophys. Res.-Atmos., 107, ACH 16-11-ACH 16-22, 2002.
590 Jeong, C.-H., Hopke, P. K., Kim, E., and Lee, D.-W.: The comparison between thermal-optical
591 transmittance elemental carbon and Aethalometer black carbon measured at multiple monitoring sites,
592 Atmos. Environ., 38, 5193-5204, 2004.
593 Kang, H., Zhu, B., Su, J., Wang, H., Zhang, Q., and Wang, F.: Analysis of a long-lasting haze episode in
594 Nanjing, China, Atmos. Res., 120, 78-87, 2013.
595 Krasowsky, T.S., McMeeking, G.R., Wang, D.B., Sioutas.C., Ban-Weiss, G.A.: Measurements of the
596 impact of atmospheric aging on physical and optical properties of ambient black carbon particles in Los
597 Angeles, Atmos. Environ., 142, 496-504, 2016.
598 Katrinak, K. A., Rez, P., Perkes, P. R., and Buseck, P. R.: Fractal geometry of carbonaceous aggregates
599 from an urban aerosol, Environ. Sci. Technol., 27, 539-547, 1993.

带格式的：字体：11 磅

Khoder, M.: Atmospheric conversion of sulfur dioxide to particulate sulfate and nitrogen dioxide to particulate nitrate and gaseous nitric acid in an urban area, Chemosphere, 49, 675-684, 2002.

Kleinman, L. I., Daum, P. H., Lee, Y. N., Senum, G. I., Springston, S. R., Wang, J., Berkowitz, C., Hubbe, J., Zaveri, R. A., and Brechtel, F. J.: Aircraft observations of aerosol composition and ageing in New England and Mid‐Atlantic States during the summer 2002 New England Air Quality Study field campaign, J. Geophys. Res.-Atmos., 112, 2007.

Lack, D. A., Langridge, J. M., Bahreini, R., Cappa, C. D., Middlebrook, A. M., and Schwarz, J. P.: Brown carbon and internal mixing in biomass burning particles, P. Natl. Acad. Sci. USA., 109, 14802-14807, 10.1073/pnas.1206575109, 2012.

Langridge, J. M., Lack, D., Brock, C. A., Bahreini, R., Middlebrook, A. M., Neuman, J. A., Nowak, J. B., Perring, A. E., Schwarz, J. P., and Spackman, J. R.: Evolution of aerosol properties impacting visibility and direct climate forcing in an ammonia‐rich urban environment, J. Geophys. Res.-Atmos., 117, 2012.

Lei, T., Zuend, A., Wang, W., Zhang, Y., and Ge, M.: Hygroscopicity of organic compounds from biomass burning and their influence on the water uptake of mixed organic–ammonium sulfate aerosols, Atmos. Chem. Phys., 14, 11625-11663, 2014.

Lewis, K., Arnott, W. P., Moosmüller, H., and Wold, C. E.: Strong spectral variation of biomass smoke light absorption and single scattering albedo observed with a novel dual‐wavelength photoacoustic instrument, J. Geophys. Res.-Atmos., 113, 2008.

Li, C., Marufu, L. T., Dickerson, R. R., Li, Z., Wen, T., Wang, Y., Wang, P., Chen, H., and Stehr, J. W.: In situ measurements of trace gases and aerosol optical properties at a rural site in northern China during East Asian Study of Tropospheric Aerosols: An International Regional Experiment 2005, J. Geophys. Res.-Atmos., 112, 2007.

Li, J., Pósfai, M., Hobbs, P. V., and Buseck, P. R.: Individual aerosol particles from biomass burning in southern Africa: 2, Compositions and aging of inorganic particles, J. Geophys. Res.-Atmos., 108, 2003.

624 Li, W., and Shao, L.: Transmission electron microscopy study of aerosol particles from the brown hazes in
625 northern China, J. Geophys. Res.-Atmos., 114, 2009.
626 Li, W., and Shao, L.: Direct observation of aerosol particles in aged agricultural biomass burning plumes
627 impacting urban atmospheres, Atmos. Chem. Phys., 10, 10589-10623, 2010.
628 Li, W., Shao, L., and Buseck, P.: Haze types in Beijing and the influence of agricultural biomass burning,
629 Atmos. Chem. Phys., 10, 8119-8130, 2010.
630 Li, W., Shao, L.: Characterization of mineral particles in winter fog of Beijing analyzed by TEM and SEM.
631 Environ. Monit. Assess., 161, 565-573, 2010.
632 Moffet, R. C., Desyaterik, Y., Hopkins, R. J., Tivanski, A. V., Gilles, M. K., Wang, Y., Shutthanandan, V.,
633 Molina, L. T., Abraham, R. G., and Johnson, K. S.: Characterization of aerosols containing Zn, Pb, and Cl
634 from an industrial region of Mexico City, Environ. Sci. Technol., 42, 7091-7097, 2008.
635 Moffet, R. C., and Prather, K. A.: In-situ measurements of the mixing state and optical properties of soot
636 with implications for radiative forcing estimates, P. Natl. Acad. Sci. USA., 106, 11872-11877, 2009.
637 Pathak, R. K., Yao, X., and Chan, C. K.: Sampling artifacts of acidity and ionic species in $PM_{2.5}$, Environ.
638 Sci. Technol., 38, 254-259, 2004.
639 Peppler, R., Bahrmann, C., Barnard, J. C., Laulainen, N., Turner, D., Campbell, J., Hlavka, D., Cheng, M.,
640 Ferrare, R., and Halthore, R.: ARM Southern Great Plains site observations of the smoke pall associated
641 with the 1998 Central American fires, B. Am. Meteorol. Soc., 81, 2563-2591, 2000.
642 Qian, Y., Wang, W., Leung, L. R., and Kaiser, D. P.: Variability of solar radiation under cloud‐free skies
643 in China: The role of aerosols, Geophys. Res. Lett., 34, 2007.
644 Quan, J., Zhang, Q., He, H., Liu, J., Huang, M., and Jin, H.: Analysis of the formation of fog and haze in
645 North China Plain (NCP), Atmos. Chem. Phys., 11, 8205-8214, 2011.
646 Ram, K., Sarin, M., and Tripathi, S.: Temporal trends in atmospheric PM2. 5, PM10, elemental carbon,
647 organic carbon, water-soluble organic carbon, and optical properties: impact of biomass burning emissions
648 in the Indo-Gangetic Plain, Environ. Sci. Technol., 46, 686-695, 2012.

带格式的：字体：11 磅

649 Ramana, M., Ramanathan, V., Feng, Y., Yoon, S., Kim, S., Carmichael, G., and Schauer, J.: Warming
650 influenced by the ratio of black carbon to sulphate and the black-carbon source, Nat. Geosci., 3, 542-545,
651 2010.
652 Ramanathan, V., Crutzen, P. J., Lelieveld, J., Mitra, A., Althausen, D., Anderson, J., Andreae, M., Cantrell,
653 W., Cass, G., and Chung, C.: Indian Ocean Experiment: An integrated analysis of the climate forcing and
654 effects of the great Indo-Asian haze, 2001.
655 Ramanathan, V., Chung, C., Kim, D., Bettge, T., Buja, L., Kiehl, J., Washington, W., Fu, Q., Sikka, D.,
656 and Wild, M.: Atmospheric brown clouds: Impacts on South Asian climate and hydrological cycle, P. Natl.
657 Acad. Sci. USA., 102, 5326-5333, 2005.
658 Ramanathan, V., Ramana, M. V., Roberts, G., Kim, D., Corrigan, C., Chung, C., and Winker, D.: Warming
659 trends in Asia amplified by brown cloud solar absorption, Nature, 448, 575-578, 2007.
660 Roden, C. A., Bond, T. C., Conway, S., and Pinel, A. B. O.: Emission factors and real-time optical
661 properties of particles emitted from traditional wood burning cookstoves, Environ. Sci. Technol., 40, 6750-
662 6757, 2006.
663 Saleh, R., Adams, P.J., Donahue, N.M., Robinson, A.L.,: The interplay between assumed morphology and
664 the direct radiative effect of light-absorbing organic aerosol, Geophys. Res. Lett. 43, 8735–8743, 2016.
665 Seinfeld, J. H., and Pandis, S. N.: Atmospheric chemistry and physics: from air pollution to climate change,
666 John Wiley & Sons, 2012.
667 Shi, Z., Shao, L., Jones, T. P., Whittaker, A., Lu, S., Berube, K. A., He, T., and Richards, R. J.:
668 Characterization of airborne individual particles collected in an urban area, a satellite city and a clean air
669 area in Beijing, 2001, Atmos. Environ., 37, 4097-4108, 2003.
670 Shi, Z. B., D. Z. Zhang, H. Z. Ji, S. Hasegawa, and M. Hayashi.: Modification of soot by volatile species
671 in an urban atmosphere, Sci. Total Environ., 389, 195–201, 2008.
672 Shingler, T., Sorooshian, A., Ortega, A., Crosbie, E., Wonaschütz, A., Perring, A.E.: Ambient observations
673 of hygroscopic growth factor and f(RH) below 1: Case studies from surface and airborne measurements, J.
674 Geophys. Res., 121, 13661-13677, 2016.

带格式的：字体：11 磅

675 Solomon, S.: Climate change 2007-the physical science basis: Working group I contribution to the fourth
676 assessment report of the IPCC, Cambridge University Press, 2007.
677 Stanmore, B., Brilhac, J., and Gilot, P.: The oxidation of soot: a review of experiments, mechanisms and
678 models, Carbon, 39, 2247-2268, 2001.
679 Sun, Y., Zhuang, G., Tang, A., Wang, Y., and An, Z.: Chemical characteristics of PM2. 5 and PM_{10} in haze-
680 fog episodes in Beijing, Environ. Sci. Technol., 40, 3148-3155, 2006.
681 Takemura, T., Nakajima, T., Dubovik, O., Holben, B. N., and Kinne, S.: Single-scattering albedo and
682 radiative forcing of various aerosol species with a global three-dimensional model, J. Climate., 15, 333-
683 352, 2002.
684 Tan, H.B., Liu, L., Fan, S.J., Li, F., Yin, Y., Cai, M.F., Chan, P.W., 2016. Aerosol optical properties and
685 mixing state of black carbon in the Pearl River Delta, China, Atmos. Environ., 131, 196-208, 2016.
686 Wang, G., Kawamura, K., Xie, M., Hu, S., Cao, J., An, Z., Waston, J. G., and Chow, J. C.: Organic
687 molecular compositions and size distributions of Chinese summer and autumn aerosols from Nanjing:
688 Characteristic haze event caused by wheat straw burning, Environ. Sci. Technol., 43, 6493-6499, 2009a.
689 Wang, H., He, C., Morawska, L., McGarry, P., and Johnson, G.: Ozone-initiated particle formation, particle
690 aging, and precursors in a laser printer, Environ. Sci. Technol., 46, 704-712, 2012a.
691 Wang, R., Tao, S., Wang, W., Liu, J., Shen, H., Shen, G., Wang, B., Liu, X., Li, W., and Huang, Y.: Black
692 carbon emissions in China from 1949 to 2050, Environ. Sci. Technol., 46, 7595-7603, 2012b.
693 Wang, X., and Chen, J.: Fog Formation in Cold Season in Ji’nan, China: Case Analyses with
694 Application of HYSPLIT Model, Adv. Meteorol., 2014, 8, 10.1155/2014/940956, 2014.
695 Wang, X., Xu, B., and Ming, J.: An overview of the studies on black carbon and mineral dust deposition in
696 snow and ice cores in East Asia, J. Meteorol. Res., 28, 354-370, 10.1007/s13351-014-4005-7, 2014.
697 Wang, Y., Zhuang, G., Sun, Y., and An, Z.: The variation of characteristics and formation mechanisms of
698 aerosols in dust, haze, and clear days in Beijing, Atmos. Environ., 40, 6579-6591, 2006.
699 Wang, Y., Che, H., Ma, J., Wang, Q., Shi, G., Chen, H., Goloub, P., and Hao, X.: Aerosol radiative forcing
700 under clear, hazy, foggy, and dusty weather conditions over Beijing, China, Geophys. Res. Lett., 36, 2009b.

带格式的：字体：11 磅，下标
带格式的：字体：11 磅

Wu, D., Mao, J., Deng, X., Tie, X., Zhang, Y., Zeng, L., Li, F., Tan, H., Bi, X., and Huang, X.: Black carbon aerosols and their radiative properties in the Pearl River Delta region, Science in China Series D: Earth Sciences, 52, 1152-1163, 2009.

Xia, X., Chen, H., Wang, P., Zhang, W., Goloub, P., Chatenet, B., Eck, T., and Holben, B.: Variation of column‐integrated aerosol properties in a Chinese urban region, J. Geophys. Res.-Atmos., 111, 2006.

Yan, P., Tang, J., Huang, J., Mao, J., Zhou, X., Liu, Q., Wang, Z., and Zhou, H.: The measurement of aerosol optical properties at a rural site in Northern China, Atmos. Chem. Phys., 8, 2229-2242, 2008.

Yang, M., Howell, S., Zhuang, J., and Huebert, B.: Attribution of aerosol light absorption to black carbon, brown carbon, and dust in China–interpretations of atmospheric measurements during EAST-AIRE, Atmos. Chem. Phys., 9, 2035-2050, 2009.

Yu, X., Cheng, T., Chen, J., and Liu, Y.: A comparison of dust properties between China continent and Korea, Japan in East Asia, Atmos. Environ., 40, 5787-5797, 2006.

Zhang, R., Khalizov, A. F., Pagels, J., Zhang, D., Xue, H., and McMurry, P. H.: Variability in morphology, hygroscopicity, and optical properties of soot aerosols during atmospheric processing, P. Natl. Acad. Sci. USA., 105, 10291-10296, 2008.

Zhang, W., Zhuang, G., Guo, J., Xu, D., Wang, W., Baumgardner, D., Wu, Z., and Yang, W.: Sources of aerosol as determined from elemental composition and size distributions in Beijing, Atmos. Res., 95, 197-209, http://dx.doi.org/10.1016/j.atmosres.2009.09.017, 2010.

Table 1 Details about the analysed samples on the sampling time, instantaneous meteorological state and the number of particle analysed in each sample.

Sampling Time (BST[a])			Conditions	RH	Temp.	Wind		Visibility	No.
Date	Starting	Duration		(%)	(°C)	Speed (m/s)	Direction	(km)	
25-05-2012	13:40	4 min	Clear	20	29	2	160	-	136
30-05-2012	9:31	16 min	Clear	29	24	7	350	-	92
02-06-2012	9:00	1 min	Mist[b]	83	20	4	180	2	146
02-06-2012	13:27	2 min	Clear	48	27	4	190	-	138
03-06-2012	10:13	15 s	Fog	88	22	1	variable	1.2	110
18-06-2012	18:52	2 min	Haze	55	29	3	140	3	172
19-06-2012	9:10	2 min	Haze	61	25	1	variable	2.8	120
21-06-2012	9:10	1 min	Haze	69	26	2	110	2.2	117
23-06-2012	12:45	2 min	Mist[b]	84	25	4	120	3	142

[a]Beijing standard time (8 h prior to GMT).

[b]Mist is studied here as fog.

Figure captions

Figure 1. 5 episodes categorization. EP-1features haze induced mainly from transportation of south industrial pollution, EP-2 clear, EP-3 frequent transition among haze, fog and clear conditions, EP-4 clear with rain interrupted, and EP-5 haze resulted mainly from the biomass burning.

Figure 2. The 3-day back-trajectory clusters of each episode, arriving at Beijing at the height of 100 m, together with the fire spot distribution of these periods.

Figure 3. TEM typical views of the particles in clear (upper panel), haze (middle panel) and fog episodes (bottom panel). 9 components are marked with the colourful arrows. (a1) (b1) (c1) (d1) (e1) (f1) is obtained before the electron exposure and (a2) (b2) (c2) (d2) (e2) (f2) is after exposure. A fraction of S-rich particles and other unstable particles decompose after electron exposure.

Figure 4. 9 categories of particles under the TEM view. The inserted spectra are obtained by the EDS, and the grid like images are acquired from the SAED. (a) S-rich, (b)N-rich, (c)mineral. (d)K-rich, (e)soot, (f)tar ball, (g)organic, (h)metal, (i)fly ash.

Figure 5. Variation of optical parameters during the study period. (a) Total Aerosol optical depth (AOD), and AOD resulted from Mie scatter and Rayleigh scatter; (b) Ångström exponent (å) computed from the pairs of 700 nm and 450 nm, 700 nm and 550 nm, and 550 nm and 450 nm; (c) light extinction, absorption and scattering coefficients; (d) calculated single scattering albedo (SSA).

Figure 6. Percentages of 9 particle components under clear, haze and fog conditions with different mixing states.

Figure 7. BC concentrations converted from the data measured by AE-31 and MAAP. Good correlation is observed.

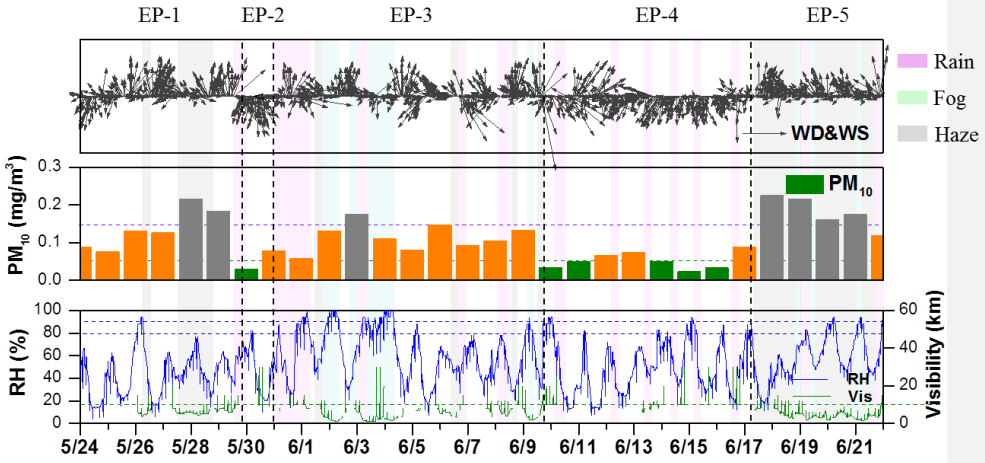
EP-1
EP-2
EP-3
EP-4
EP-5
Rain
Fog
Haze
WD&WS
PM10
PM10 (mg/m3)
0.3
0.2
0.1
0.0
RH (%)
100
80
60
40
20
0
Visibility (km)
60
40
20
0
RH
Vis
5/24
5/26
5/28
5/30
6/1
6/3
6/5
6/7
6/9
6/11
6/13
6/15
6/17
6/19
6/21

Figure 1

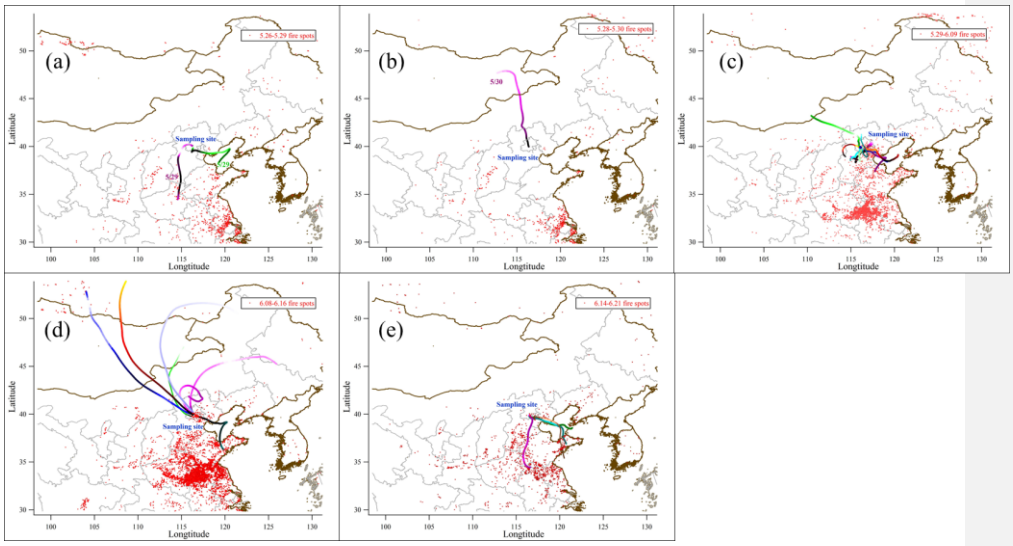
(a)
5.26-5.29 fire spots
Sampling site
5/26
5/29
(b)
5.28-5.30 fire spots
5/30
Sampling site
(c)
5.29-6.09 fire spots
Sampling site
(d)
6.08-6.16 fire spots
Sampling site
(e)
6.14-6.21 fire spots
Sampling site
Latitude
Longtitude

Figure 2

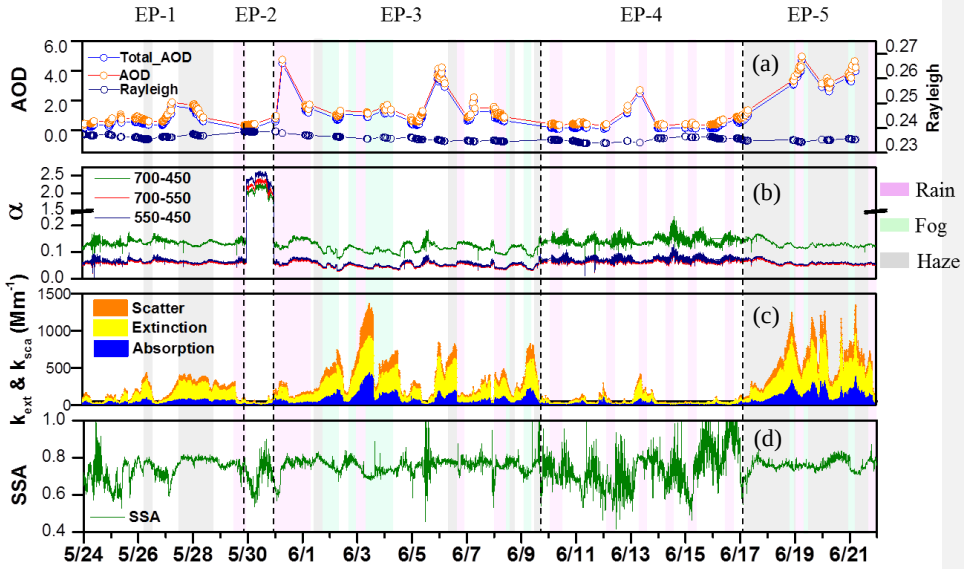
EP-1
EP-2
EP-3
EP-4
EP-5
AOD
Total_AOD
AOD
Rayleigh
(a)
Rayleigh
α
700-450
700-550
550-450
(b)
Rain
Fog
Haze
k_{ext} & k_{sca} (Mm^{-1})
Scatter
Extinction
Absorption
(c)
SSA
SSA
(d)
5/24
5/26
5/28
5/30
6/1
6/3
6/5
6/7
6/9
6/11
6/13
6/15
6/17
6/19
6/21

Figure 3

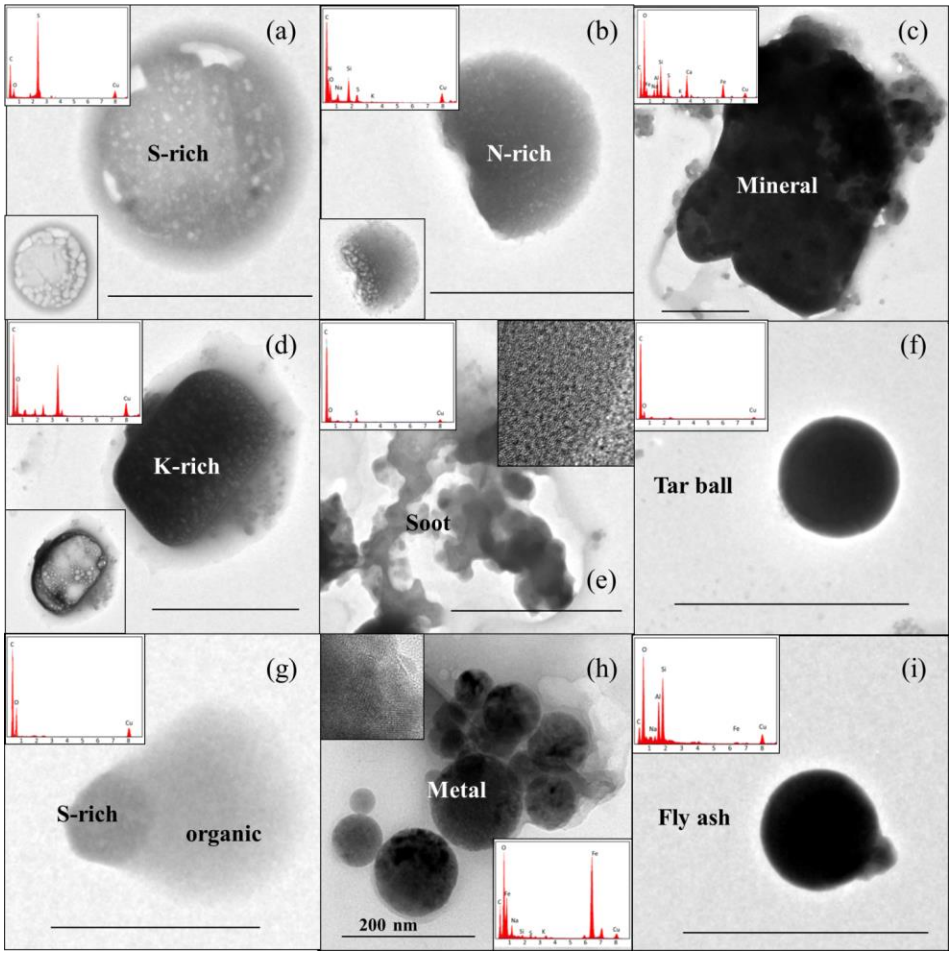
(a)
S-rich
(b)
N-rich
(c)
Mineral
(d)
K-rich
(e)
Soot
(f)
Tar ball
(g)
S-rich
organic
(h)
Metal
200 nm
(i)
Fly ash

Figure 4

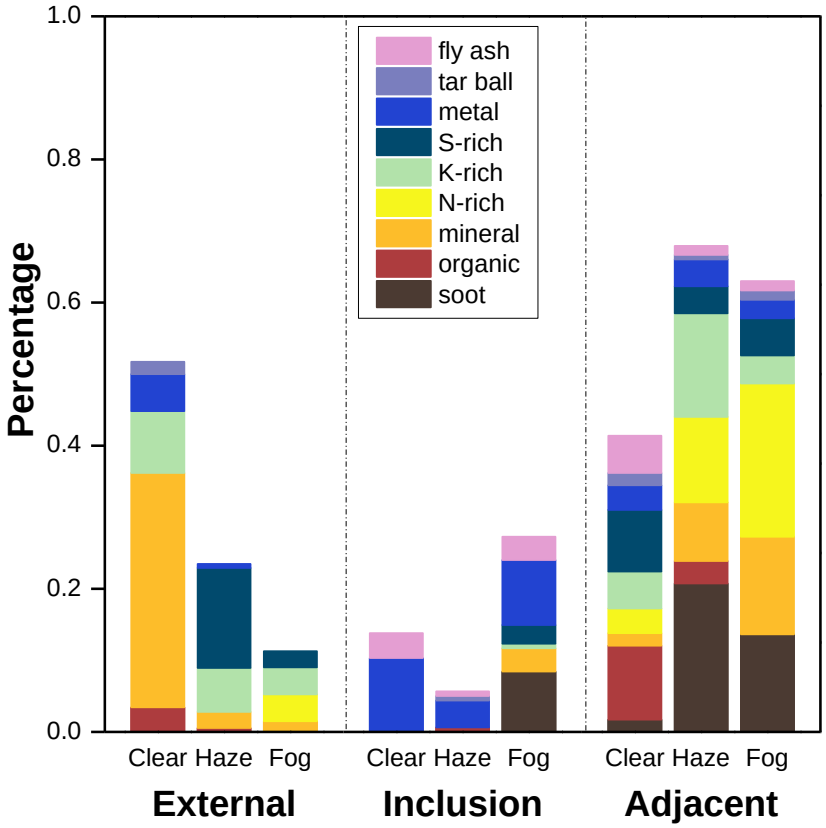

785

786

787

788 **Figure 5**

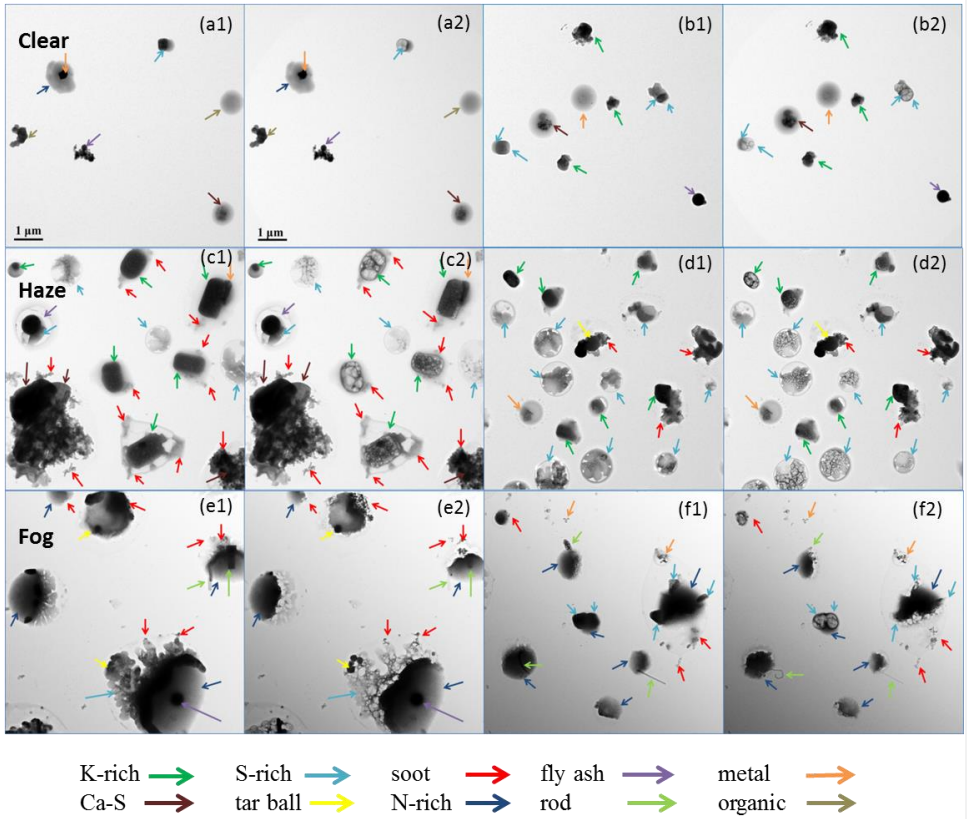

789

790

791

792

793

794 **Figure 6**

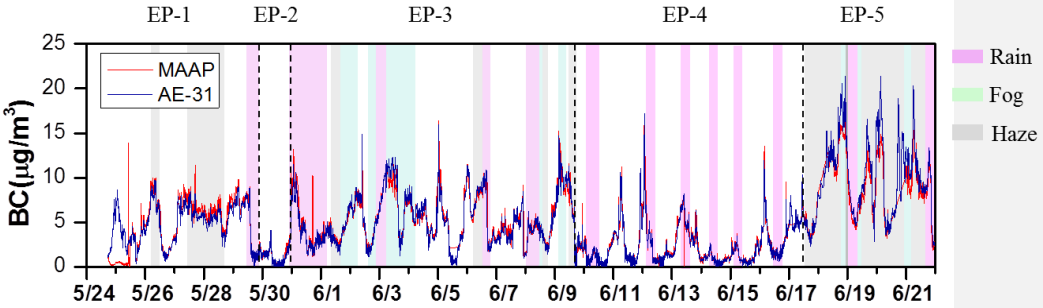

795

796

797

798

799

800

801

802

803

804 **Figure 7**

805